Hylonome

Form follows function: a computational simulation exercise on bone shape forming and conservation

U. Mittag[1], A. Kriechbaumer[1], M. Bartsch[2], J. Rittweger[2,3]

[1]German Aerospace Center, Institute for Aerospace Medicine, Linder Höhe, 51147 Köln, Germany;
[2]German Aerospace Center, Institute of Materials Research, Linder Höhe, 51147 Köln, Germany;
[3]Institute for Biomedical Research into Human Movement and Health, Manchester Metropolitan University, Manchester, United Kingdom

Abstract

The present paper explores whether the shape of long bone shafts can be explained as a mere result of mechano-adapation. A computer simulation study was conducted in order to investigate adaptation processes of bone-like structures under load patterns comparable to those acting on the diaphysis of long bones. The aim of the study was to have a deeper look into the relationship between typical loading patterns and resulting bone shape and structure. The simulations are based on a mechanistic model approach for mechano-transduction and bone transformation. Results of the simulations are that axial torsion around the long axis is important for the evolvement and maintenance of tube-like structures. Of note such structures can form from a variety of starting geometries, provided that axial torsion is present. The selection of the set-point parameter for the regulation of load adapted bone transformation has an impact on the final structure as well. In conclusion, the present study confirms the mechanical environment's potential to generate shaft-like structures and demonstrates the respective boundary conditions.

Keywords: Bone Adaptation, Mechanostat, *In Silico* Study, Structural Mechanics, Bone Modelling

Introduction

The seemingly inert bone of vertebrates is, in reality, a living tissue that retains adaptive capability throughout the lifespan[1,2]. Transformation of bone in response to alterations of its mechanical environment is evident in numerous examples, e.g. from the bone loss observed during space flight and bed rest[3,4] as well as their recovery[5,6]. Such adaptive modifications of bone are often engendered by alterations in geometry, both during immobilization[7] as well as in sport-specific responses to increased loading[8-10].

However, even when there is no net gain or loss in bone mass, it is evident that a continuous process of bone renewal takes place, which is often called remodelling[2]. This process involves resorption of bone plus subsequent formation, and it is thought to be partly of random nature and partly specifically targeted to repair tissue damaged by micro-cracks[11]. Disorders of these mechanisms are held responsible for bone disorders such as osteoporosis[12] and osteogenesis imperfecta[13], and a deeper understanding will be a prerequisite for effective therapeutic strategies. It is conceivable that these mechanisms also relate to the bone loss of astronauts, and that understanding them will enable the design of effective countermeasures.

In principle, mechanically driven adaptive responses of human bone had been observed and described early by Wolff[14], later known as "Wolff's Law" of bone transformation, and it was d'Arcy Thompson who coined the principle 'form follows function'[15]. Pauwels explained quite well how load forces could determine certain characteristics of the geometry of human long-bones[16]. Frost proposed the mechanostat theory to explain bone adaptation as a feed-back control mechanism[17,18]. His 'three-way rule' that proposes shifts of the bone surface depending on different on-off criteria explains the observations in principle but does not yet have a quantitative mechanistic background. The early authors distinguish strictly between 'modelling' and 'remodelling', with the former describing the shaping of bones and prevailing during growth, and the latter describing the self-renewal of bone that prevails

during adulthood[1,2]. It has been recognized that these processes do not occur simultaneously, and the idea therefore emerged that they are biologically distinct.

Evidence suggests that osteocytes, living cells embedded in the bone matrix, play a crucial role in mechano-sensation and transduction of the mechanical signals[19]. Another finding was that dynamic bone loading (i.e. incorporating frequent load changes) is more effective at inducing bone adaptation processes than static loading[20]. With this background in mind Huiskes and co-workers created a Finite Element Analysis (FEA) based computer model for remodelling processes within trabecular bone that used a mechanistic approach with a strong cell-biological background of bone adaptation[20,21]. In their remodelling law they assume the osteocytes in the bone matrix to be the main control element for the recruitment and bone generating activity of osteoblasts. They are postulated to take strain energy density as the leading regulatory parameter for the mechano-transduction.

Early studies have looked upon the diaphysis of long bones and their optimal shape studying interspecies diversity[22] and investigating the adaptive response of different load types like compression, bending, and torsion on the cross section with numerical methods[23-25]. However, these studies have accepted a tubular shape a priori. The influence of axial torsion for the adaptation of cross section parameters was in most cases found to be limited[23,26]. Torsion did not play a role in numerical models to explain flexure-neutralization[27].

It is a known fact in orthopaedic surgery that bones can remedy their misalignment after fracture (so-called flexure neutralization). However elegant the past studies on bone shaping are, they do not have a mechanistic explanation for it. It is not understood whether bones look the way they do because they are used the way they are used, or vice versa. Or, in other words: whether form follows function or function follows form, and to what macroscopic extent bone is a self-organizing tissue is yet to be established. Of course, there might be also a genetic background, but overwhelming evidence suggests that function can explain the form to a large extent.

The goal in this study is to link tissue-level adaptive responses to whole-bone shaping in order to understand why bones are shaped the way they are. For this we are focussing on the basic principles responsible for reshaping of bone-like structures in response to loading. The present approach uses computer modelling to perform experiments of thoughts on a simplified level. Accordingly, we present work based upon simplistic geometries. The underlying transformation scheme, however, is kept close to physiological patterns. The algorithm originally proposed by Huiskes for the remodelling domain has been adapted in this study, in order to show that the principles are the same for modelling and remodelling. In order to foster that vision and to avoid confusion with the historical terminology we use the term transformation for both modelling and remodelling in this paper.

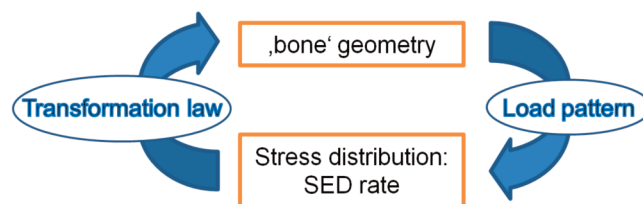As a first step, we describe a bone shaft analogue both in terms of physiologically-motivated boundary conditions as well as in terms of code implementation. We hypothesize that a bone shaft- analogue load pattern will generate a straight tube-like compact structure from different precursor geometries, showing that the straight tube in full three dimensions - that obviously seems to be the optimum structure - is supported by the adaptation laws on microbiological level, and that it is not only an adaptation of an existing tubular cross section. If the straight tube is the preferred geometry, then one should expect (as our secondary hypothesis), that flexed precursor geometries should be straightened as suggested by flexure neutralization in clinical observations. Both hypotheses presume that form follows the function of bone and bone parts, and therefore loads are one of the main drivers of bone anatomy.

Figure 1. Transformation cycle.

Methods

The *in silico* transformation cycle used here assumes that mechanic loads are guiding the transformation process. The cycle (Figure 1) starts from a given model geometry, where a random load pattern comparable to those acting on the diaphysis of long bones is then applied. Next, the resulting stress distribution within the structure is calculated by means of Finite Element Analysis (FEA) using the commercial FEA software ANSYS. The distribution of strain energy density rate in the volume elements of the model is the control parameter of this "mechanostat" and is the input for the transformation algorithm, which results in a modification of the model geometry. With this modified geometry the process is re-iterated step by step. The details are explained in the following.

The geometry models were defined within a design space, which is structured by a regular cubic voxel mesh with an edge length of 75 voxels. The housing mesh size was 4.5x4.5x4.5 mm^3, bringing the voxel length to 0.06 mm. The elements (voxels) in this mesh were either defined as isotropic bone material with a compact bone-like Young's modulus, or of non-bone character with Young's modulus two orders of magnitude less. Following Huiskes' example, structures similar to a primary spongiosa were defined as regular grid inside the cubic design space with a regular and homogeneous pattern of bone. In this approach non-bone elements also have to be calculated by the FEA algorithm. Therefore the design space was selected to be only slightly larger than the objects to be analysed. The resolution was restricted by computer resources. With its 421875 elements the model approach is a good compromise.
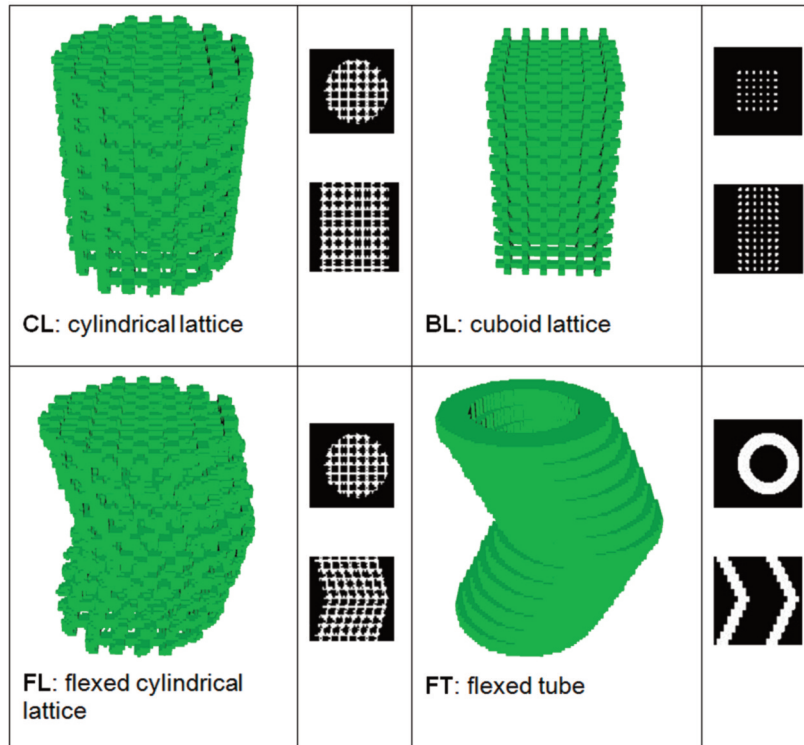
Figure 2. Starting geometries; for all four different starting geometries CL, BL, FL and FT a 3D-view (+y/-z-view, x-axis horizontally) together with cross-section representations in the xy-plane (top) and in the xz-plane (bottom) are shown (x-axis horizontally): CL a cylindrically shaped Bravais lattice, BL a cuboidal shaped cubic Bravais lattice (box lattice), FL a cubic Bravais lattice in form of a flexed cylinder and FT a flexed tube; find more explanations in the text.

A total of four different starting geometries was used (see Figure 2). In one direction (z-direction) the geometries extended over the entire design space, while in the other directions the geometries did not touch the design space edges, in order to leave space for apposition. One exception was the flexed geometries that touched the outer edges at 3 points. The following starting geometries were used:

CL: a cylindrical shaped cubic Bravais lattice with the axial length of the full design space size of 4.5 mm and a width of 3.38 mm. This was the main geometry to observe the transformation from spongious to compact geometry.

BL: a quadratic cuboid sized Bravais lattice (box lattice) with the length of the full design space size of 4.5 mm and diameter of 2.25 mm. This was the geometry that we used to focus on transformation of outer shape. We intentionally chose smaller dimensions in comparison to geometry 1 in order to get an idea, if there might be an influence on the final dimensions. Also the unit cell of the lattice has been modified (see explanation below).

FL: a flexed cylindrical Bravais lattice with the length of the full design space size of 4.5 mm and a diameter of 3.38 mm. The degree of flexion was sufficient to let the flexed geometry occupy the whole design space in a mediolateral direction. This geometry will show if flexure neutralization from flexed spongious structure is possible.

FT: a flexed cylindrical tube with the length of the full design space size of 4.5 mm and a diameter of 3.38 mm. With this geometry we want to find out if flexure neutralization is also possible starting from flexed compact structures.

The unit cell of our cubic lattices in CL and FL is a cube of an edge length of 8 voxels (= 0.48 mm) with beams of 2x2 voxels at all edges building a cubic frame. Putting together that kind of unit cells, a cubic lattice of quadratic beams of width 4 voxels (=0.24 mm) is generated. The unit cell of BL is different in having a width of 6 voxels (0.36 mm) with one voxel sized beams at all edges building a lattice with thinner beams of 2x2 voxels (0.12 mm) width. In all cases we used a template lattice generated in Matlab and matched that lattice into the mesh of our FE model using ANSYS standard functionality. Irregular surfaces of the lattice rods are due to this matching process. The irregularity was assumed not to influence the simulation results, because for one type of starting geometry always the same lattice was used for all runs. The flexed starting geometries were used to investigate the flexure neutralization problem.

The dimensions studied here are downscaled for technical reasons in comparison to human scales. They are similar to that of a rat femur. Therefore, we kept the mechanical properties similar to rat conditions. We assumed isotropic mechanical properties for the compact bone. The value for Young's mod-

ID	Z (ax.) [N]	XY (lat.) [N]	Torque [Nmm]	k_{tr} [10^{-2} nmol/ (mm²*day)]	#steps	Starting geometry
CL0	-100	40	+/-180	250	200	CL
CL1	-100	40	+/-180	120	200	CL
CL2	-100	40	+/-180	50	200	CL
CL3	-100	40	+/-180	20	200	CL
CL4	-100	40	+/-180	5	400	CL
CL5	-100	40	0	5	200	CL
CL6	-100	40/90°	+/-180	5	200	CL
CL7	-100	40/90°	0	5	200	CL
BL1	-100	40	+/-180	5	200	BL
BL2	-100	40	0	5	200	BL
FL1	-100	40	+/-180	5	200	FL
FL2	-100	40	0	5	200	FL
FT3	-100	40	+/-180	5	400	FT
FT4	-100	40	0	5	400	FT

Table 1. Overview of the computational runs performed in this study. Z gives the axial compressional force, XY the bending forces. Torque is the torque around the z-axis. Values for k_{tr} are given as well as step number per run and starting geometry. Every run has got an identifier (ID) that indicates its starting geometry. See Figure 2 for explanation of the acronyms CL,BL,FL and FT.

ulus of 15000 MPa for cortical bone was in line with our reference[21] and similar to the observed range from 16000 to 19000 MPa for rat cortical bone[28]. For rat cortical bone poisson numbers between 0.3 and 0.42 were found[29], so we took 0.36 as a mean for our simulations.

For simulation of mechanical loads the geometry models were implemented in the Finite Element simulation software ANSYS (ANSYS Germany GmbH, Darmstadt) version 12.1. In this numerical model each voxel is represented by a brick element with quadratic shape function. For the load calculations the geometry's bottom and top surfaces (with respect to the z-direction) were fixed to rigid plates. The bottom plate was fixed in three directions, and the surface of the top plate was subjected to different types of loads such as axial compression, varying lateral bending and torque (details are given in Table 1). For this purpose the ANSYS basic functions 'external force' and 'moment' on a rigid surface have been used. The scripting capability of ANSYS Workbench has been used to modify both the external force vector as well as the torque vector of the ANSYS-'moment' in subsequent calculation steps in order to simulate the variance of the load pattern (Figure 3).

We estimated the rat load conditions by scaling down known load conditions of the human case, because measurements of real loads on these animals *in vivo* are incomplete in the literature. From force measurements in smart knee prostheses[31] one can derive load conditions on human long bones in non-sporting activities. There we find maxima of 350% body weight (BW) for axial load (knee load in z-direction ~ axial load on tibia), some 2% BWm torque around z-axis (can be taken as the axial torque on the tibia) as well as shear forces in the knee up to 40% BW (can be taken as bending forces for the tibia). For a rat of 1kg we can scale that to 35 N axial load, 4 N bending load and 0.2 Nm (200 Nmm) axial torque. For running and jumping the
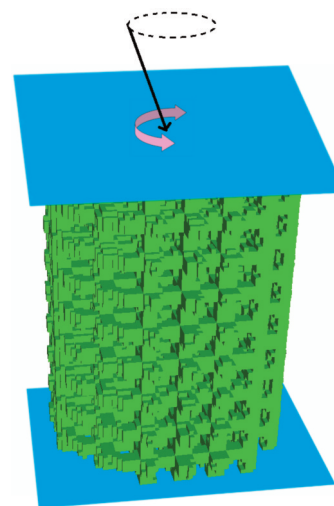

Figure 3. Load pattern for diaphysis models (see explanation in the text).

loads will be much higher, especially the bending load, because higher dynamic forces will come into effect. Therefore, as depicted in Figure 3, a constant major compressive force in axial direction with a magnitude of 100 N was applied on the rigid top surface and modulated by a smaller component in lateral direction. The lateral force was taken as random in direction with a constant magnitude (40 N in all cases, see details in Table 1). In Figure 3 the resulting force sum on the top plate is depicted as a black arrow, the dashed circle visualizing the random direction in 360°. In order to study the influence of lateral bending components that are non-uniformly distributed we narrowed the possible random direction down to a 90° segment in two of the

runs. The magenta arrow in Figure 3 represents an additional random torque around the length axis of the model. At any step it can assume any value between a maximum clockwise and counter-clockwise magnitude (uniformly distributed). The absolute values of the maxima in both directions are identical, comparable in magnitude to values for rat long bones above. In all cases where torque was present, 180 Nmm as the maximum magnitude (see Table 1 for details) was taken.

The transformation law has been adopted from Huiskes et al.[20,21] and simulates the modification of bone density m (value between 0 and 1) in terms of the bone-generating activities of the osteoblasts and the bone-resorbing activities of osteoclasts. Following Huiskes et al., strain energy density (SED) rate was taken as the leading mechanical signal that activates the osteocytes. In the following the algorithm proposed by this group is described:

The modification of bone density m_{tot} at time t and location x is given by positive contributions of osteoblasts m_{bl} and negative contributions of osteoclasts m_{cl}:

$$\frac{dm_{tot}(x,t)}{dt} = \frac{dm_{bl}(x,t)}{dt} - \frac{dm_{cl}(x,t)}{dt} \tag{1}$$

The osteoblast contributions are given by:

$$\frac{dm_{bl}(x,t)}{dt} = \tau\,(P(x,t) - k_{tr}), \tag{2}$$

for $P(x, t) > k_{tr}$, disappears for $P(x, t) <= k_{tr}$

$$P(x,t) = \sum_{i=1}^{n} f(x, x_1)\mu_1 R(x_1,t), \tag{3}$$

with $f(x, x_i) = e^{-d(x, xi)/D}$

where index i indicates the osteocytes in the neighbourhood.

P is a trigger signal at a surface position and depends on the distances between osteocytes (given by $f(x,x_i)$), the sensitivities of the osteocytes (given by μ_i) and the SED rates (given by $R(x_i,t)$). As can be seen from equation (2), there is a threshold parameter k_{tr} that makes sure, that the system only reacts on P-values that reach a certain level. Below that level bone resorption does not occur. τ is an additional gain factor.

$R(x_i,t)$ calculates from $S(x_i,t)$ as given in equation (4), the SED and a load frequency of F, the latter taken as 1 for typical walking-like load pattern:

$$R(x_i, t) = 4.08\,S(x_i, t)\,F \tag{4}$$

This formula results if we look at a load $\sigma_e(t)$ oscillating with frequency F, taking values between 0 and a maximum value σ. If we follow the derivation of Ruimerman[21] we can calculate the maximum SED S_{max}:

$$S_{max} = max\left(\frac{1}{8}K\sigma^2\,(1+\cos(2\pi Ft))^2\right) = \frac{1}{2}K\sigma^2 \tag{4a}$$

The corresponding maximum SED rate can be calculated as
$$R_{max} = 0.65\pi FK\sigma^2 \tag{4b}$$

Assuming that a single step corresponds to several days in reality and our $S(x_i,t)$ is the S_{max} of the oscillating load pattern during that time, we can take over formula 4a for $S(x_i,t)$ and analogous equation 4b for $R(x_i,t)$. Comparing both equations we find the relationship of equation 4.

We calculated $P(x,t)$ for up to seven shells of voxels neighboring a surface voxel. For this calculation we had to take into account the number of osteocytes per voxel that we took as 44000 per mm³ as for human cortical bone[21], the number of

voxels and the number of osteocytes per voxel defining the total number of osteocytes (the N of equation 3) taken into account.

From m(x,t) the Young's modulus E(x,t) can be calculated as $E_{max}\cdot m^\gamma$ with in our case $E_{max} = 15000$MPa and $\gamma=3$ (see reference[21]).

For the resorption Huiskes et al. give:
$$\frac{dm_{cl}(x,t)}{dt} = r_{cl} \tag{5}$$

where r_{cl} is a statistical value, wherein the recruitment rate of osteoclast cavities (in [1/voxel/day]) on the surface (f_{ocl}) and the resorbed volume per cavity (v_r) play a role.

We calculated the voxel resorption rate as:
$$\frac{d_{vox}}{day} = f_{ocl}\left(\frac{v_r}{v_{vox}}\right) c_{corr} \tag{6}$$

with v_{vox} the voxel volume. For better comparability with the Huiskes calculations we use a correction factor $c_{corr} = (dx/dx_{huis})^2$, where dx, dx_{huis} are the voxel sizes of our model and the Huiskes reference model. Because only surface voxels are involved, we have to correct Huiskes f_{ocl} parameter (recruitment rate of bone modeling units BMU) for our differing voxel sizes in two dimensions (always looking at the surface).

We did not take into account coupling between osteoclast and osteoblast-activity and assume a random distribution of osteoclast activity over the whole surface.

The transformation cycle was implemented in Matlab (Mathworks Inc., Natick, Mass. USA) version R2011a. Strain energy densities resulting from the simulated load applications were calculated using FEA based on the commercial package ANSYS, using a Preconditioned Conjugate Gradient (PCG) solver. Calculations were performed on a high performance computing cluster (IBM x3550 and X iDataPlex computers). For each run, between 200 and 400 iterations were calculated before we could be sure, that the forming process had converged. Our criteria for convergence are given in detail in the results section below. Each calculation step (a single loop of the transformation cycle) took around 60 minutes.

In pre-calculations it had been found that the given threshold k_{tr} had to be adapted significantly in order to achieve an activation of the process. When varying the magnitude of k_{tr} it appeared that the value of this parameter has a big impact on the final geometry in dynamic equilibrium. To better understand the underlying systematics, we performed several additional computational runs in order to check the sensitivity for this parameter. As a result for further simulation experiments we selected a setting of $k_{tr}=0.05$ nmol/(mm²·day), because this value provided a good tubular shape in the basic load configuration.

An overview of all runs is given in Table 1.

A total of eight runs was performed with the cylindrical lattice (CL) as starting geometry (identifier CLx with x=0....7). In five of them (CL0 to CL4) we varied the Huiskes threshold parameter keeping other parameters constant. In run CL5 we set the torsional load to zero with all other parameters unchanged. In run CL6 we kept the bending load in a narrow angle of 90 degrees (into the quadrant of positive x- and y-direction) in order to see any influence of directed bending. In run CL7 we combined directing bending forces as in CL6 with missing tor-
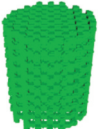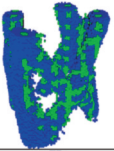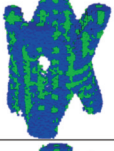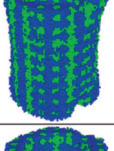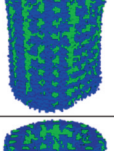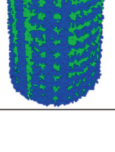
ID	Starting geometry (3D-view, left; cross sections mid-shaft and axial, right)	Final geometry (3D view, left; cross sections mid-shaft and axial, right)	Outer radius R mid-shaft [mm]	R/t mid-shaft
CL0			n/a	n/a
CL1			n/a	n/a
CL2			n/a	n/a
CL3			n/a	n/a
CL4 (200 steps)			1.7$^{+/-}$0.1	2.3$^{+/-}$0.2
CL4 (600 steps)			1.7$^{+/-}$0.1	2.4$^{+/-}$0.2

Figure 4a. Results for runs CL0 to CL4; same presentation as in Figure 2 with starting geometries always a 3D view together with two cross-sections; original voxels in green, new voxels in blue.

sional loads. In all CL-runs 200 steps have been calculated except for CL4, where we extended to 400 steps in order to demonstrate the stability of the final geometry. In addition two runs with the box lattice (BL) as starting structure (BL1, BL2) have been performed to investigate the dependence on the starting geometry. Again one of them was without torsional load (BL2). In order to investigate the flexure problem four runs have been calculated, two starting from the flexed cylindrical lattice (FL), the other two starting from the flexed tubular structure (FT), in both cases once with torsion and once without.

Table 2 shows an overview of the parameter settings in the Huiskes algorithm that have been used in all calculations.

In order to be able to compare to earlier investigations on bone shaft geometries we calculated the radius R of the final shaft geometries as well as the parameter R/t, with t being the thickness of the corticalis.

Parameter	Setting	Dimension
τ	5.10^{-7}	mm^5/(Nmol)
D	100	μm
μ (osteocyte)	1	nmol·mm·s/(J·day)
F	1	Hz
V_r	1.5	mm^3
f_{ocl}	$7.1·10^{-4}$	1/(voxel·day)
days/step	30	
osteocyte density	44.10^3	1/mm^3

Table 2. Constant settings of important parameters of the Huiskes model (equations 2-4); with given dimensions, the $R(x_i,t)$- resp. the $S(x_i,t)$-values from the FEM results have to be entered in GPa.
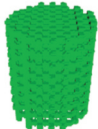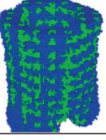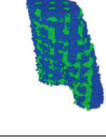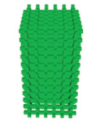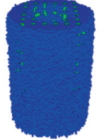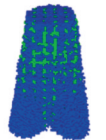
ID	Starting geometry (3D-view, left; cross sections mid-shaft and axial, right)		Final geometry (3D view, left; cross sections mid-shaft and axial, right)		Outer radius R mid-shaft [mm]	R/t mid-shaft
CL5					n/a	n/a
CL6					1.7⁺/⁻0.1	2.8⁺/⁻0.5
CL7					n/a	n/a
BL1					1.6⁺/⁻0.1	2⁺/⁻0.2
BL2					n/a	n/a

ID	Starting geometry (3D-view, left; cross sections mid-shaft and axial, right)		Final geometry (3D view, left; cross sections mid-shaft and axial, right)		Outer radius R mid-shaft [mm]	R/t mid-shaft
CL5					n/a	n/a
CL6					$1.7^{+/-}0.1$	$2.8^{+/-}0.5$
CL7					n/a	n/a
BL1					$1.6^{+/-}0.1$	$2^{+/-}0.2$
BL2					n/a	n/a

Figure 4b. Results for runs CL5 to CL7 and for runs BL1 and BL2; same color code as in Figure 4a.
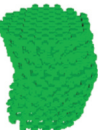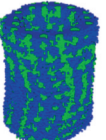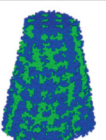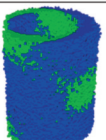
ID	Starting geometry (3D-view, left; cross sections mid-shaft and axial, right)		Final geometry (3D view, left; cross sections mid-shaft and axial, right)		Outer radius R mid-shaft [mm]	R/t mid-shaft
FL1					$1.65^{+/-}0.1$	$2.5^{+/-}0.2$
FL2					n/a	n/a
FT1					$1.65^{+/-}0.1$	$2.5^{+/-}0.2$
FT2					n/a	n/a

Figure 4c. Results for runs FL1, FL2, FT1, FT2; same color code as in Figure 4a.

For convergence checking several indicators have been calculated for the mid-shaft slice (at 2.25 mm in z-direction) that give an idea of topological modifications with time. The indicators were:

1. Number of bone voxels
2. Mean radius
3. Standard deviation of bone voxels from mean radius
4. The two principle moments of area
5. Optically assessed shape
6. Deviation index I_d

The deviation index I_d was calculated using formula (8).

$$I_d = \sum_x \sum_y (E(t2,x,y) - E(t1,x,y))^2 / (\sum_x \sum_y E(t1,x,y))^2 + \sum_x \sum_y E(t2,x,y))^2) \qquad (8)$$

with $E(t1,x,y)$ and $E(t2,x,y)$ being the Young's moduli at two different times at the same position x, y of the mid-shaft slice. This index vanishes in case of identity and becomes 1 for 100% deviation.

Results

In the tables of Figures 4a-c results of our computations are presented as 3D-visualizations and as silhouettes of a mid-shaft cross-section on the top right and an axial cross-section on the bottom right in the 3rd column. For comparison the starting geometry is shown as well in 3D as in the cross-sectional silhouettes in the 2nd column. The 3D-pictures show green and blue voxels, the green ones being 'bone' voxels that survived from the beginning, the blue ones being voxels that have been generated during the simulation. The two remaining columns show the outer radius and, for comparison with literature[22], the R/t value at mid-shaft only for cases where a regular tube can be identified at mid-shaft. Because of the rough surface of structures the measurement of diameters and wall thickness could not be very precise, thus we provided an estimate for the variation.

Quick convergence was found after about 200 calculation steps for all lattice-type starting geometries. For the flexed tube starting geometry it took longer to reach equilibrium. Therefore, we extended the runs to 400 steps in these cases.

Figure 5 shows as an example the run CL4 to demonstrate that within about 100 to a maximum of 200 steps the system has reached its final geometry. The characteristic parameters have attained a level that will be kept more or less stable (radius, standard deviation of radius) or with a small drift (moments of area and bone voxel number). Voxel number and moments of area show a noticeable oscillation. It can be easily seen, that the moments of area vary in phase with the voxel number. The I_d-value converges quickly to a quite low but non-zero value.

Looking into the results of the different runs, a strong shape-imposing influence was found for the threshold values k_{tr}. As can be seen from equation 2, this threshold defines a minimum value, below which an integrated trigger signal on a surface position does not activate bone formation. First calculations with a high setting for this value provided truss-like final structures. Systematic variation in k_{tr} in this study yielded a close relationship between this parameter and structural properties,
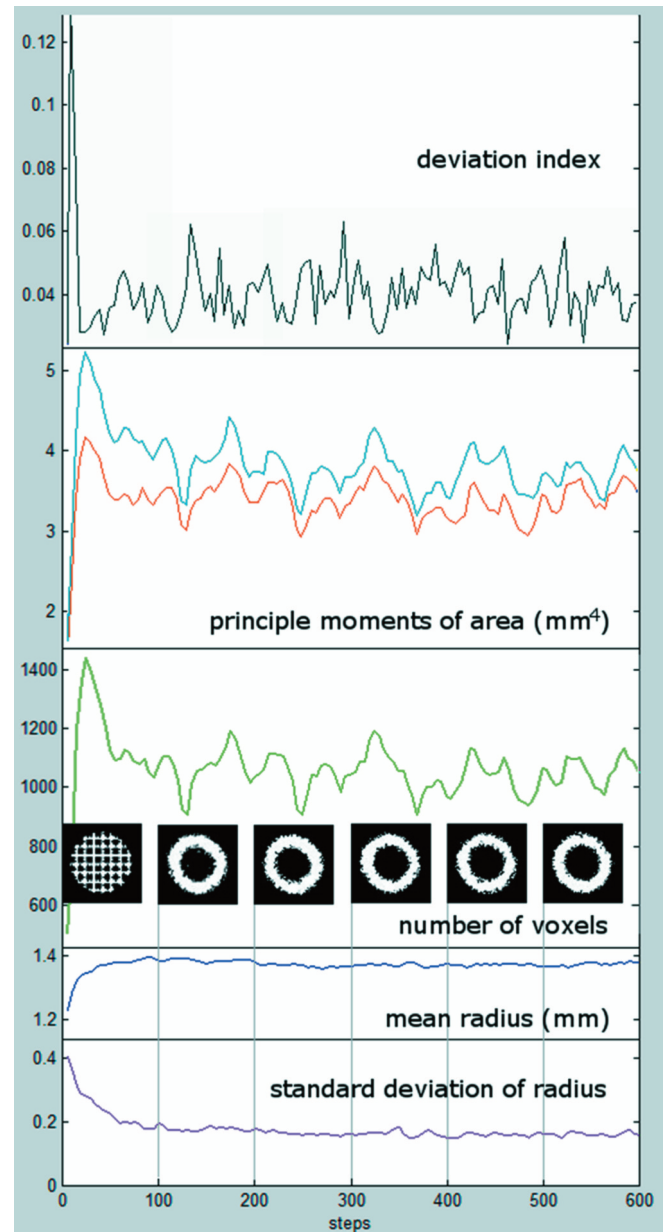
Figure 5. Monitoring of parameters of slice 37 (mid-shaft) during an ultra-long run of 600 steps of experiment CL4 as a function of the step number; lower part: number of bone voxels (green), mean radius (blue) and its standard deviation (magenta); upper part: deviation index (black) and the both principle moments of area (light blue and brown); in addition silhouettes of cross-sections at step 0, 100, 200, 300 400, 500 are given.

which can be seen easily by comparing the final geometries of the runs CL1 to CL4 in the table of Figure 4a. From a closed straight tube for k_{tr}=0.05 nmol/(mm²·day) the structure opens up and broadens more and more at the ends of the tube with increasing magnitude of k_{tr} and finally grows into the open truss-like form at k_{tr}=1.2 nmol/(mm²·day). The beams of the truss seem to become more filigree with further increasing magnitude of k_{tr}.

Looking more closely now at CL4, where we used the low value for k_{tr}, we observed the conversion of our spongious starting geometry to a closed and straight tubular structure with a clear "corticalis". This tube wall is very regular in thickness. The diameter stays close to the diameter of the original geometry.

In CL5 (see table in Figure 4b) we run the same conditions without the axial torsional load component. As it can be clearly seen, the final geometry is no longer tubular, but has the form of a truncated cone. The mid shaft cross section has smaller diameter and an irregular shape compared to the torsional loaded run.

CL6 and CL7 (see table in Figure 4b) show the effects of introducing a strongly directed bending load towards one of the quadrants. The quadrant in question is marked by a red angle in the mid shaft cross section representation. It can be seen that with torsional load in CL6 we got a geometry that is not far from that of uniform distributed bending in CL4. There is a slightly increased thickness of the tube wall in this quadrant, but the effect is much less than could be expected. The anticipated effect arises, when torsion is 'off', as can be seen in CL7. Here we have a completely different picture - no tubular geometry at all, indicating an important role of torsion for maintaining the tube.

In BL1 (results in table of Figure 4b) we used the same conditions as in CL4, but started from the quadratic (instead of a circular) cross section of starting scheme BL with quite a small diameter in comparison to the start setting of CL4. From a cuboid starting lattice we again got a tubular geometry. The final outer diameter was only slightly smaller (1.6 instead of 1.7 mm). The difference can be found in the much thicker tube wall resulting in a R/t value of 1.6.

BL2 that started with same conditions as BL1 but, analogue to CL5, without torsional load showed a similar behavior as CL5 (see table in Figure 4b).

From our flexed starting geometries FL1, FL2, FT1, FT2 we extracted the following results shown in Table 3c: FL1 (the flexed spongiosa as initial geometry), after 200 steps, results in a regular straight tubular structure that is very similar to that of the comparable CL4 run, which started in unflexed configuration. For FT1, which started from a flexed tube configuration, the effect and the resulting geometry is a straight tube as well, but a bit less regular as with the "spongiosa" based FL1.

When torsional loads are switched off we find, when starting from a spongy structure (example FL2), a final geometry very similar to the results of runs CL5 and BL2, namely a truncated cone. When starting from the flexed tube (example FT2) the behaviour is different. We do not get a truncated cone-shaped structure which we may have expected when comparing it to the flexed lattice case FL2. There seems to be a trend to narrow the upper diameter. But it can be stated in any case: a closed straight tube does not develop.

Different from the smooth surfaces of long bones in nature the surfaces of all of our final geometries show a considerable degree of roughness.

Discussion

It is the principle goal of this publication to establish an *in silico* platform for testing of bone transformation laws and to use it to identify possible mechanisms and laws on the mesoscopic level that are able to explain the phenomenological laws established by Frost from a mechanistic point of view.

As the first study in this context the present study tried to explain common geometrical transformations of bone (e.g. spongy to compact as in the metaphysis during growth, or flexure neutralization) mainly on the basis of a transformation law that has been proposed for the mechanically-driven remodelling of trabecular bone. Investigating principles in an experiment of thought, we focus on a construct that has sufficient similarity to the shaft of a long bone of a rat from the viewpoint of load characteristics. Even with this sparse approach, a number of remarkable results have been achieved.

Before discussing the results let us first come back to general aspects and some differences of the present model approach with respect to the Frost mechanostat. Due to the 'bottom-up' approach that we used in order to study bone as a self-organizing tissue, our simulations did not take into account a merit function or any other 'determination' constraint, other than regulation by local strains and stresses. The fact that even in the absence of such constraining assumptions, our simulations found R/t-values that are very similar to those reported by Currey and Alexander for land mammals[22] may add to the applicability of our results. We are aware that the transformation law under investigation has been proposed only for adaptation processes based on bone basic multicellular units (BMU) next to marrow at trabecular and endocortical surfaces. In this study it was applied generally for all surfaces including the periosteal ones, so that we reduced the two different mechanisms of Frost (modeling and remodeling) to a single mechanism. In contrast to Frost's definition, the present model has only one single 'modelling' set-point, the already mentioned k_{tr}. The model relies on a steady bone absorption like a thermostat that only needs one set-point in a cold climate, because there is always heat dissipation and no active cooling is required. It is astonishing how already this single-set-point set-up can manage an effective mechano-adaptation. In our future investigations, it will certainly be important to have a closer look whether this set-up can also explain the findings of a lazy zone and if that is not the case to identify a set-point mechanism for the active cooling (meaning active reduction of bone mass in case of disuse) analogous to bone.

Resuming the results we find the following:

1. In line with our main hypothesis the 'typical' load pattern assumed for long bones in combination with a generalized modelling/remodelling transformation algorithm based on reasonable assumptions on bone physiologic principles supports the formation and maintenance of regular and straight tubular structures.

2. In line with our secondary hypothesis this kind of formation of regular straight tubular structures is independent of the starting geometry and therefore also holds for flexed geome-

tries, leading to flexure neutralization.

3. The findings 1) and 2) are valid under certain boundary conditions: a) the set-point-values used in the calculation are in a well-defined range, otherwise truss-like open structures arise; b) axial torsional loads have to be present; otherwise a variety of geometries form that are not straight or tubular.

4. Bending loads into a selected direction do not deform the tubular shape very much. The thickness of the wall is thicker on the loaded side. Again this statement loses its validity if torsion is missing.

5. The independence of starting geometry of finding 2) holds for the tubular shape, but not for the dimensions of the resulting cross-sections with respect to radius and wall thickness.

6. Rough surfaces develop in our simulations in comparison to smooth surfaces in reality.

Thus, and in line with the initial hypothesis, mechano-adaption occurred from different starting conditions - spongy, non-cylindrical and flexed geometries, implying that load patterns typical for a bone shaft evoke the well-known tubular structure with closed compact bone in the "cortical" area. In the first instance this looks self-evident. Other authors in the literature have taken this principal geometry as given and looked on dimensional variations[22], or investigated variations of the cross sectional geometry[25]. In this study we consequently applied the 'form follows function' principle and assumed load as the main shape defining and maintaining entity. The results suggest that tubular shape is not self-evident. It is a more surprising outcome that the presence of axial torsion was crucial, not to say required in order to achieve realistic shaft structures. In the literature torsion normally plays a minor role. In the work of Mittlmeier[26] the authors found out in a computational study that torsion cannot explain deviations from the ideal tube. Indeed torsion does not explain deviations, but it seems to ensure that the base geometry is the tube. If one takes tubular shape as given and only looks on a thin cross section, as those authors did, then you will find no influence of torsion. This is underlined when looking on the cases of this study where directed bending is involved. Here we find only a minor impact on the thickness of the tubular wall when torsion is in place, but break-down of the tube without torsion. Others[30] came to very similar results when they simulated the development of a long bone cross section when directed bending was effective. The tube shape was lost if not compensated by taking the degree of calcification of the bone tissue into account.

We do not see other computational studies where the influence of torsion has been an issue. The reason for that might be that torsional loads in long bones could not be measured very well *in vivo* and therefore have been neglected or taken of minor influence. It is only recently that data have been obtained from smart prostheses after knee replacement[31,32] that show that axial torques are present. These values[31] have been taken as reference for our own simulations (see above). A recent experimental *in vivo* study from our group has yielded that also in healthy young people axial torsion of substantial magnitude is present during locomotion[33].

If we assume that the anatomy of bone is optimized for the load it experiences and want to learn why it has this shape we have to look closely into the regimes in our model where we find deviations. Beside the missing torsion we find a high value of the threshold parameter k_{tr} as a possible reason. At first glance that seems to be a more technical aspect of the simulation, but we have to be aware that the parameter k_{tr} plays the role of the modeling set-point in the sense of the Frost mechanostat because it rules the onset of bone adsorption. In our model it also seems to be an important determinant for bone shape building. The higher the set-point with respect to the magnitude of the loads or in reverse the lower the forces with respect to the set-point the more the system seems to prefer deviation from the ideal tube to truss-like open geometries. Such structures are often found in engineering and structural biology (e.g. trabecular bone material), but are not typical for a complete bone. An explanation for this behaviour might be that higher set-points are more selective. If there are small local differences in the stress pattern, the slightly higher stressed areas will be very selectively reinforced. Reinforced areas draw additional load and reduce stress in other areas so that this differentiation is amplified.

If we translate this virtual phenomenon into relevance for real bone adaptation processes we should consequently expect that disuse based osteoporosis in a long bone shaft should tend to be irregular in the sense that areas already weakened are candidates for enhanced bone reduction. But of course at this point we should not forget that we have simplifications in our models. E.g., taking anisotropy of bone material properties into account might change conditions. Future *in silico* and *in vivo* studies will help to clarify this. For another open question our set-point phenomenon might be relevant as well, namely the question why spongy (resp. truss-like) structures are preferred in the epiphyseal region of the bone. Is it only because other types of forces, especially shear forces, are becoming dominant there, or is it because we are in a lower force regime with respect to the set-point?

The truss-structures that result from the structure optimizing process of remodeling strongly resemble principles that have been applied in engineering for many years as "method of biologic growth" in Computer Aided Optimization (CAO), the latter being derived from principles learned from tree growth[34]. It is not really a surprise that what is good for nature in finding optimized structure in tree growth could also be a major principle in bone growth and adaptation.

We have found that under the given load conditions, if torsion is present and the set-point is in the right range, straight tubular geometry is achieved independently of the starting geometries be it a cylindrical or a cuboid lattice or even a flexed lattice or tube. Especially, the straightening - or 'flexure-neutralization' - could not be expected. In his classic experiment of thought, Frost had argued that the mechanostat theory alone cannot explain flexure-neutralization, and he had therefore partly waived his theory and postulated a 'marrow factor' that identified or symbolized whole-bone compression[18]. It is interesting, therefore, that taking the mechanostat idea to a truly quantitative level the mechanostat can be rec-

onciled with flexure neutralization. With this finding we are in line with the outcomes of Roberts et al.[27] in their computational study using a different contour based simulation approach. This states that the straightening of askew healed bone in fast modelling and remodelling bones as seen in the bones of children can be explained as driven by load, thereby suggesting that the guiding influence is bone adsorption to bone surfaces near high strain energy areas.

Looking at parameters like radius of the tube or thickness of the wall we find differences depending on starting conditions. While the radius is quite similar, the C/t value starting from cuboid lattice with smaller diameter is with 2.0 significantly smaller than the values of the other runs starting from other lattices lying around 2.4. The reason for this is a thicker tube wall. This behaviour is difficult to explain.

Why do we see such rough surfaces in our final structures, rather than the smooth kind of surfaces seen in nature? This is equally true for the "endocortical" as well as for the "periosteal" surfaces, which is rather unsurprising as the mechanisms in our model are identical for both. This is related to the fact that the simulation can only adapt by adding and removing little cubes. By chance the volume of the voxel in the present simulation ($2.2*10^{-4}$ mm^3) is quite similar to the v_r, the typical size of a BMU cavity ($1.5*10^{-4}$ mm^3). However, in reality the BMU cavities are not cubes, but flat and elongated pits. In addition the simulation finds its position completely randomly on the surface, so it might happen that a voxel is taken away where there is already a pit in existence, leading to ragged surfaces with pits up to 2 voxel sizes deep. In principle, this could be improved by much better resolution both in space and time, as both temporal and spatial resolution are quite coarse in these simulation experiments. In this sense a smoother surface can be expected when enhancing the grid resolution to below that of the BMU size. The temporal resolution of our model (30-days per step) only allows for resolving the delta in bone adsorption and resorption during an entire BMU activity. Modelling resorption in smaller time steps will undoubtedly lead to smoother surfaces, but would by far exceed current computing limitations.

Thus, in conclusion, the present exercise, although initiated as a first approach, has yielded interesting results in that a remodeling law without any specific assumptions on surface-organization like in the 'three-way rule' can explain mechano-adaptation in terms of compactization, corticalization, circularization, and flexure neutralization. Of the many variations possible in our computer model, we have identified appropriate setting of k_{tr}, the threshold parameter of bone formation, as well as application of torsional loads as powerful stimuli. This outcome makes us believe that numerical implementation of mechano-adaption is a fruitful field of research, and it is intended to prepare a platform, where we can invite other investigators to use our tools and to join our efforts on this field.

Having investigated a very narrow aspect of bone mechano-adaptation, a logical next step will be to study the epiphyseal region of long bones, too. First results reveal problems arising from the different scales of macroscopic shape forming and mesoscopic trabecular transformation, which we are currently trying to consolidate with a two scale approach looking at high resolution trabecular spots inside a matrix of coarser resolution structures at the macroscopic level.

References

1. Frost HM. Skeletal structural adaptations to mechanical usage (SATMU): 1. Redefining Wolff's law: the bone modeling problem. Anat Rec 1990;226(4):403.
2. Frost HM. Skeletal structural adaptations to mechanical usage (SATMU): 2. Redefining Wolff's law: the remodeling problem. Anat Rec 1990;226(4):414.
3. Vico L, Collet P, Guignandon A, Lafage-Proust MH, Thomas T, Rehaillia M, Alexandre C. Effects of long-term microgravity exposure on cancellous and cortical weight-bearing bones of cosmonauts. Lancet 2000; 355(9215):1607-1611.
4. Rittweger J, Frost HM, Schiessl H, Ohshima H, Alkner B, Tesch P, Felsenberg D. Muscle atrophy and bone loss after 90 days of bed rest and the effects of flywheel resistive exercise and pamidronate: results from the LTBR study. Bone 2005;36(6):1019-1029.
5. Rittweger J, Felsenberg D. Recovery of muscle atrophy and bone loss from 90 days bed rest: Results from a one-year follow-up. Bone 2009;44(2):214-224.
6. Sibonga JD, Evans HJ, Sung HG, Spector ER, Lang TF, Oganov VS, Bakulin AV, Shackelford LC, LeBlanc AD. Recovery of spaceflight-induced bone loss: bone mineral density after long-duration missions as fitted with an exponential function. Bone 2007;41(6):973-978.
7. Biggin A, Briody JN, Ramjan KA, Middleton A, Waugh MA, Munns CS. Evaluation of bone mineral density and morphology using pQCT in children after spinal cord injury. Dev Neurorehabil 2013;16(6):391-397.
8. Haapasalo H, Kontulainen S, Sievaenen H, Kannus P, Jaervinen M, Vuori I. Exercise-induced Bone Gain Is Due to Enlargement in Bone Size Without a Change in Volumetric Bone Density: A Peripheral Quantitative Computed Tomography Study of the Upper Arms of Male Tennis Players. Bone 2000;27(3):351-357.
9. Wilks DC, Winwood K, Gilliver SF, Kwiet A, Chatfield M, Michaelis I, Sun LW, Ferretti JL, Sargeant AJ, Felsenberg D, Rittweger J. Bone mass and geometry of the tibia and the radius of master sprinters, middle and long distance runners, race-walkers and sedentary control participants: A pQCT study. Bone 2009;45:91-97.
10. Ireland A, Maden-Wilkinson T, McPhee J, Cooke K, Narici M, Degens H, Rittweger J, , Upper limb muscle-bone asymmetries and bone adaptation in elite youth tennis

players, Med Sci Sports Exerc 2013;45(9):1749-1758.

11. Burr DB, Martin RB, Schaffler MB, Radin EL. Bone re-modeling in response to *in vivo* fatigue microdamage. J Biomech 1985;18(3):189-200.

12. Schonau E, Schwahn B, Rauch F. The muscle-bone relationship: methods and management - perspectives in glycogen storage disease. EurJ Pediatr 2002;161(Suppl 1):50.

13. Rauch F. Material matters: a mechanostat-based perspective on bone development in osteogenesis imperfecta and hypophosphatemic rickets. J Musculoskelet Neuronal Interact 2006;6(2):142-146.

14. Wolff J. Das Gesetz der Transformation der Knochen. Berlin: Hirschwald; 1892. Translated by Manquet P and Furlong R as The Law of Bone Remodelling. Berlin: Springer; 1986.

15. Thompson DA. On Growth and Form. Cambridge: Cambridge University Press; 1917.

16. Pauwels F. Biomechanics of the locomotor apparatus: contributions on the functional anatomy of the locomotor apparatus. Berlin, New York: Springer;1980.

17. Frost HM, Bone "mass" and the "mechanostat": a proposal. Anat Rec 1987;219(1):1-9.

18. Frost HM. Wolff's law: an 'MGS' derivation of Gamma in the Three-Way Rule for mechanically controlled lamellar bone modelling drifts. Bone and Mineral 1993;22:117-127.

19. Turner CH., Forwood MR, Otter MW. Mechanotransduction in bone: do bone cells act as sensors of fluid flow? FASEB J 1994;8(11): 875-878.

20. Huiskes R, Ruimerman R, van Lenthe GH, Janssen JD. Effects of mechanical forces on maintenance and adaptation of form in trabecular bone. Letters to Nature 2000; 400:704-706.

21. Ruimerman R. Modeling and Remodeling in bone tissue, Proefschrift, Technical University Eindhoven, ISBN 90-386-2856-0; 2005.

22. Currey JD, Alexander RMcN. The thickness of the walls of tubular bones. J Zool Lond 1985;(A) 206: 453-468.

23. Cowin SC. Bone remodeling of diaphyseal surfaces by torsional loads: theoretical predictions. J Biomech 1987;

20(11-12):1111-1120.

24. Carter DR, Van Der Meulen MCH, Beaupré GS. Mechanical factors in bone growth and development. Bone 1996; 18(1 Suppl):5S-10S.

25. Kumar NC, Dantzig JA, Jasiuk IM, Robling AG, Turner CH. Numerical Modeling of Long Bone Adaptation due to Mechanical Loading: Correlation with Experiments. Ann Biomed Eng 2010;38(3):594-604.

26. Mittlmeier T, Mattheck C, Dietrich F. Effects of mechanical loading on the profile of human femoral diaphyseal geometry. Mol Eng Phys 1994;6(1):75-81.

27. Roberts MD, Hart RT. Shape adaptation of long bone structures using a contour based approach. Comput Methods Biomech Biomed Engin 2005;8(3):145-56.

28. Vanleene M, Rey C. Relationships between density and Young's modulus with microporosity and hysic-chemical properties of Wistar rat cortical bone from growth to senescence. Med Eng Phys 2008;30(8):1049-1056.

29. Kohles SS, Bowers JR, Vailas AC, Vanderby Jr R. Effect of Hypergravity Environment on Cortical Bone Elasticity in Rats. Calif Tissue Int 1996;59:214-217.

30. Kummer B. Grundlagen der Pauwels-Theorie der funktionellen Anpassung des Knochens. Orthopaedie 1995; 24:387-393

31. Kutzner I, Heinlein B, Graichen F, Bender A, Rohlmann A, Halder A, Beier A, Bergmann G. Loading of the knee joint during activities of daily living measured *in vivo* in five subjects. J Biomech 2010;43(11):2164-2173.

32. D'Lima DD, Patil S, Steklov N, Cowell CW. The 2011 ABJS Nicolas Andry Award: 'Lab'-in-a-Knee: *In vivo* knee forces, kinematics, and contact analysis. Clin Orthop Relat Res 2011;469:2953-2970.

33. Yang P, Sanno M, Ganse B, Koy T, Brüggemann GP, Müller LP, Rittweger J. Bending and torsion predominate the *in vivo* human tibia deformation regimes during walking and running. PLoS One 2014;9(4):e94525.

34. Mattheck C. Design in der natur – Der Baum als Lehrmeister, 3. Überarb. Und erw. Neuauflage. Freiburg im Breisgau: Rombach GmbH Druck und Verlagshaus; 1997.